Why Is the Terrestrial Water Storage in Dryland Regions Declining? A Perspective Based on Gravity Recovery and Climate Experiment Satellite Observations and Noah Land Surface Model With Multiparameterization Schemes Model Simulations

Li-Ling Chang[1] [ID], Ruiqiang Yuan[2] [ID], Hoshin V. Gupta[1], C. Larrabee Winter[1] [ID], and Guo-Yue Niu[1] [ID]

[1]Department of Hydrology and Atmospheric Sciences, The University of Arizona, Tucson, AZ, USA, [2]School of Environment and Resource, Shanxi University, Taiyuan, China

Abstract Drylands cover over 40% of the global land area and are home to more than 2 billion humans. Here, we use the terrestrial water storage (TWS) anomaly data derived from GRACE satellites to assess water storage changes globally and find that drylands lost ~15.9 ± 9.1 mm of water between April 2002 and January 2017. The TWS trends are more significant and apparent in dry regions than in humid regions. The decrease in TWS occurred mainly in hyperarid and arid regions. Exact causes to the observed declines in TWS remain elusive due to anthropogenic water withdrawals, atmospheric demand (potential evapotranspiration, *PET*) in contrast to supply (precipitation, *P*) caused by the warming, and terrestrial ecohydrological responses. Therefore, we use a process-based model forced by climate data to interpret the causes over three selected dryland regions showing the strongest drying trends. We find that the modeled TWS without considering anthropogenic water withdrawals explains most of the declining GRACE TWS over the southwestern North America (NA) and Middle East but underestimates the drying trend over North China. This suggests that TWS declines in the southwestern NA and the Middle East were primarily driven by the contrast between atmospheric demand and supply, whereas anthropogenic water withdrawals may have played a relatively more dominant role in TWS declines over North China. Additional model experiments indicate that terrestrial ecohydrological processes that help extract deep substrate water are critical for providing water supply additional to precipitation to sustain *ET* in the drying drylands at decadal scales.

1. Introduction

Drylands cover more than 40% of the global land area and support approximately 2.5 billion people (38% of the global population) (Reynolds et al., 2007). Around 90% of the dryland population lives in developing countries that lag significantly behind other areas with harsh human well-being (Safriel et al., 2005). In these regions, freshwater resources are critical for domestic use, irrigated agriculture, and economic development (Wada et al., 2010). In addition, dryland ecosystems, as the world's largest biome (Schimel, 2010), strongly depend on water resources for biological activities that are essential for ecosystem functionality and service (Delgado-Baquerizo et al., 2013). They contribute to ~40% of global net primary productivity (carbon intake by plant photosynthesis minus release by plant respiration) (Grace et al., 2006; L. Wang, D'Odorico, et al., 2012) due to their high rain use efficiency (Huxman et al., 2004; Ponce-Campos et al., 2013). Despite the apparent drying trend since 1980s, dryland ecosystems dominate the trend and interannual variability of the global terrestrial net ecosystem exchange (gross primary productivity minus the sum of ecosystem respiration and carbon release due to wildfire) (Ahlström et al., 2015; Poulter et al., 2014).

The scarce and highly variable precipitation in dryland regions, plus their relatively high atmospheric demand for evapotranspiration (*ET*), causes drylands to be stressed by climatic water deficits (Huang et al., 2016, 2017; Middleton & Thomas, 1997; Prăvălie, 2016). In a warming climate, although the actual atmospheric water vapor has increased globally (Trenberth, 2011), which is consistent with both theory and climate models, the atmospheric water vapor pressure deficit has significantly increased due to the

warming. Despite no significant changes in global average precipitation (Gu et al., 2007; Polson et al., 2013; Trenberth, 2011), the global water cycle is expected to intensify by amplifying the contrast between global dry-wet patterns (Allen & Ingram, 2002). Drylands are expected to become drier under warming conditions (Chou et al., 2009; Held & Soden, 2006), exacerbating existing water crises and posing serious challenges to water availability and cropland productivity (Safriel et al., 2005).

As a part of the Earth system (Palmer & Smith, 2014), humans in drylands respond to water scarcity by pumping deep groundwater (Famiglietti, 2014; Gleeson et al., 2012). Unsustainable rates of groundwater withdrawal have been reported in north India (Rodell et al., 2009; Tiwari et al., 2009), California's Central Valley (Famiglietti et al., 2011; Scanlon et al., 2012), central Mexico (Castellazzi et al., 2016), the Middle East (Joodaki et al., 2014; Voss et al., 2013), and North China (Feng et al., 2013). With continuously increasing demands for freshwater resources that may not be balanced by limited water supply under population growth (Safriel et al., 2005), water stress can have economic, social, and political ramifications (Famiglietti, 2014). To pursue a sustainable future for dryland habitation, it is useful to investigate the changing states of the freshwater resources over these areas and the causes to the change.

The Gravity Recovery and Climate Experiment (GRACE) satellites provide accurate estimates of combined changes in multiple components of continent-scale water balance, including water stored in biomass, snowpack, glaciers, soils, and aquifers (Landerer & Swenson, 2012; Swenson, 2012; Swenson & Wahr, 2006). GRACE terrestrial water storage (TWS) data have been widely used to assess groundwater depletion, glacier loss, sea-level rise, droughts and floods, and ecosystem responses to TWS changes (Chen et al., 2009; Du et al., 2019; Famiglietti & Rodell, 2013; Reager et al., 2016; Rodell et al., 2009). As a cumulative effect of the water fluxes (precipitation-*ET*-runoff-groundwater pumping and irrigation) (Eicker et al., 2016) over time, the signal recorded in GRACE TWS anomaly data is more reliable than the estimates of individual water flux terms. Recently, researchers have used GRACE measurements to assess decadal changes of TWS at a global scale (Humphrey et al., 2016; Reager et al., 2016; Rodell et al., 2018). As the TWS change records the combined natural and anthropogenic impacts on the water cycle, its trends reflect the responses of dryland ecohydrological processes to climate change and human interventions.

Previously, using GRACE TWS data, Scanlon et al. (2016, 2018) reported negative water storage trends in the dryland river basins of the Colorado, Rio Grande, Euphrates, and Indus but increasing trends in the Niger, Chari, Jubba, Okavango, Orange, and Murray. Focusing on arid and semiarid parts of the Middle East, Forootan et al. (2017) reported declining water storage in the Tigris-Euphrates, Persian, and Urmia basins but increasing storage in the Khazar, Markazi, Hamun, and Sarakhs basins. Negative TWS changes have been found in north India (Rodell et al., 2009; Tiwari et al., 2009), California's Central Valley (Famiglietti et al., 2011), North China (Feng et al., 2013), and northwest Australia (van Dijk et al., 2011). However, most, if not all, current macroscale hydrological models underestimate the decadal trends (either positive or negative) detected by GRACE (Scanlon et al., 2018), impeding the understanding of potential mechanisms causing the TWS changes. Therefore, the exact causes to the decreasing TWS trend remain elusive due to the combined effects of increasing atmospheric demand (potential *ET* [*PET*]) caused by the warming, water supply that are controlled by rainfall and regulated by terrestrial ecohydrological processes and anthropogenic water withdrawals.

Here we use the GRACE TWS anomaly data to evaluate the areal extent and degree of changes in water amount over global drylands and assess how apparent and statistically significant the linear trends are. While our analysis of the data includes global humid and cold regions (see section 4), we focus on dryland regions because of their "vulnerability" to changes in hydroclimatic conditions and the relatively strong signals detectable by GRACE. To interpret the GRACE TWS trends over three selected dryland regions in the midlatitudes of the Northern Hemisphere (NH), we analyze the trends in atmospheric demand and aridity index (*AI*) using the Global Land Data Assimilation System (GLDAS) near-surface hydroclimate data (Rodell et al., 2004) and a process-based land surface model (LSM), namely, the Noah LSM with multiparameterization schemes (Noah-MP; Niu et al., 2011). To discern the relative importance of the contributing factors, we conduct two model sensitivity experiments using Noah-MP with a focus on the role of two "pumping" processes: groundwater capillary rise and plant root water uptake contributing to the surface water "supply" in addition to precipitation.

2. Data

The GRACE twin satellites launched by the National Aeronautics and Space Administration (NASA) and the German Aerospace Center (DRL) in March 2002 orbit the Earth starting at an altitude of about 500 km (Tapley et al., 2004). Using a K-band microwave ranging system, the satellites sense changes in the intersatellite distance caused by the Earth's gravitational forces, thereby the strengths of fluctuations in the Earth's time-variable gravity field. The gravity fields are indicative of surface mass redistributions represented as water equivalent thickness changes.

Here, we use GRACE Level 3 product derived from spherical harmonics (SH) solutions Release 5 (RL05). The temporal and spatial evolution of TWS is processed by three centers, namely, the Center for Space Research (CSR), the Jet Propulsion Laboratory (JPL), and the GeoForschungsZentrum (GFZ). The data are available to download in geographical grid from the GRACE Tellus website. The individual time series are referred to as $GRACE_{CSR}$, $GRACE_{JPL}$, and $GRACE_{GFZ}$. All data are anomalies relative to the long-term mean field (a constant value, averaged over all months from 2004 to 2009, assigned to each grid cell). Therefore, $GRACE_{CSR}$, $GRACE_{JPL}$, and $GRACE_{GFZ}$ describe water storage deviations from the mean state at every grid cell, rather than the absolute value of water mass. Gaining or losing water relative to the mean state is represented by positive or negative values of the TWS anomalies, respectively.

In this work, we analyzed the water storage anomaly data during the period April 2002 to January 2017; note that we exclude Antarctica and Greenland. To reduce data noise associated with different processing methods (Sakumura et al., 2014), we averaged the monthly gridded values from all the three products and refer to this time series as "$\overline{G}$." Although the application of gridded gain factors restores signal amplitudes with subseasonal to seasonal frequencies, it may be inappropriate for secular trend analysis (Landerer & Swenson, 2012; Long et al., 2015). Therefore, in this study, we derived long-term trends from the mean time series $\overline{G}$ without using the gain factors. However, when comparing the time series of TWS anomalies with model simulations over three selected regions, we did apply the gain factors. Details regarding data processing are provided below and indicated on supporting information Figure S1. To confirm our conclusions with GRACE SH, we performed additional data analysis using the CSR mascons RL05 TWS (Save et al., 2016). Results using the CSR mascon are included in the supporting information.

3. Methods

3.1. TWS Linear Change Observed at Each Grid Cell

At each $1 \times 1°$ grid cell, we decomposed the averaged TWS time series $\overline{G}$ into long-term, seasonal, and residual components with the seasonal trend decomposition (STL) using Loess (Cleveland et al., 1990). Then, we computed the linear trend m_i (in mm/month) at the ith grid over the GRACE period, by fitting a least squares linear regression line to the long-term signal. By multiplying the trend value by the total number of months (178), we obtained an estimate of water storage change ($dTWS_i = 178 \times m_i$; in mm) over the whole period for each grid (Figure 1a).

We assessed the uncertainty, $Uncert_i$, in m_i, following Scanlon et al. (2018). This uncertainty accounts for (1) the solution uncertainty among the three GRACE data sets, (2) the uncertainty of the linear regression analysis, and (3) the uncertainty related with the glacial isostatic adjustment (GIA) correction. The data set uncertainty is represented by the differences among the slopes, computed as the square root of the mean squared departures of the three slopes estimated from the $GRACE_{CSR}$, $GRACE_{JPL}$, and $GRACE_{GFZ}$ time series, respectively. The linear regression uncertainty accounts for the variability in the slopes computed by the linear regression for each solution, computed as the square root of the mean squared departures of the standard errors (SEs) of the regression. The GIA uncertainty quantifies the systematic error of three competing GIA models (Caron et al., 2018; Richard Peltier et al., 2018; Tellus, 2019; Wahr & Zhong, 2012), calculated as the square root of the mean squared departures of the three GIA rates. For the ith grid cell, the combined uncertainty s_i (mm/month) is the square root of the sum of squares (RSS) of the three uncertainty sources. Finally, we multiplied the combined trend uncertainty by the total number of months (178) and obtained an estimate of water storage change uncertainty ($Uncert_i = 178 \times s_i$) in mm. Global maps showing the individual data set trend estimates (Figure S2), their SEs (Figure S3), and associated uncertainty estimates (Figures S4–S7) are provided in the supporting information.
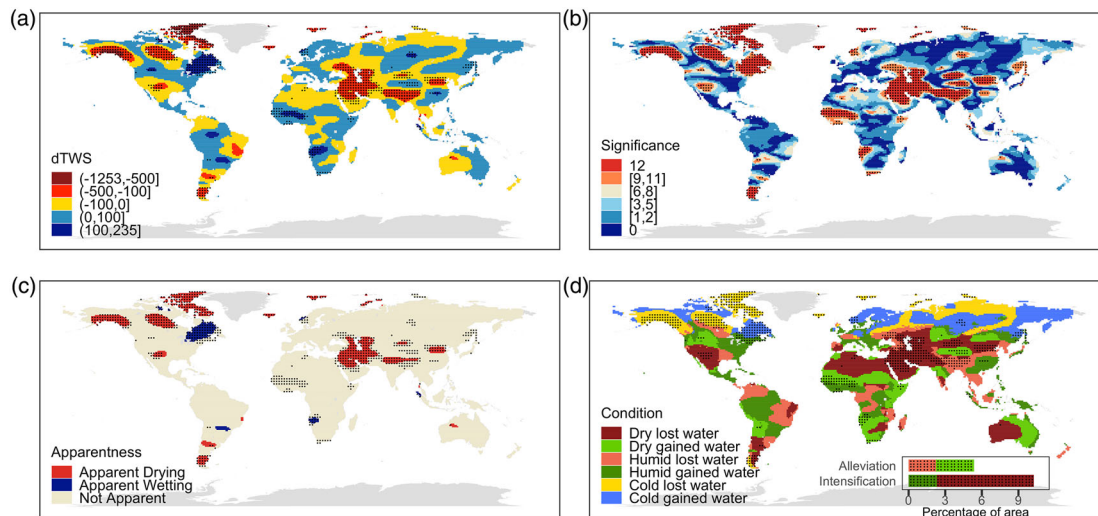
Figure 1. (a) GRACE TWS linear change (mm) from April 2002 to January 2017, (b) statistical significance by counting the number of months with TWS trends passing the significance test with α at 0.05 (values of 9 or higher are defined as statistical significant; dotted area), (c) apparentness by evaluating the value of TWS linear change and the change-to-amplitude ratio, and (d) patterns of drying and wetting of different climate regions by overlaying the GRACE TWS linear change and climate regions. Dotted areas denote regions where the long-term trends are statistically significant. In the bar plot of (d), the "dry lost water" land area is 7.9% of the global land area, "humid gained water" is 2.3%, "dry gained water" is 3.1%, "humid lost water" is 2.2%, "cold gained water" is 1.9%, and "cold lost water" is 2.8% accounting for grid cells with statistically significant trends.

3.2. Statistical Significance of TWS Linear Trends

Here, we used a novel method to determine the statistical significance of TWS linear trends at each grid cell. We first determined the observed statistical significance level of the linear trend at each grid cell, separately for each month from April 2002 to January 2017. At grid cell i, for month j, we fitted the linear regression model to data for that month. The P value (p_i^j) was estimated by the two-tailed Student's t distribution. The monthly trend with p_i^j smaller than α at 0.05 was determined as statistically significant. Then, to rate the degree of statistical significance of TWS trends at the grid cell i, we counted the number of months passing the significance test. High values imply high degree of statistical significance and vice versa. Values of 9 and higher are denoted as statistically significant. Only grid cells with statistically significant trends are included in the analysis of GRACE TWS changes in the following analysis.

3.3. TWS Annual Amplitude of Variability

To estimate the annual amplitude of the TWS variability at each grid cell, used for computing the change-to-amplitude ratio, we calculated the amplitude of the seasonal component of the decomposed time series of monthly TWS_i at grid cell i. Figure S8 presents a global map of the annual amplitude of variability.

To assess how apparent the water storage changes are, we computed the ratio ($Ratio_i$) of the TWS linear change to the TWS annual amplitude ("change-to-amplitude" ratio) at each grid cell (Figures 1c and S9) and then aggregated over the climate zones (bar plot in Figure 1c). The ratio quantifies the relative effects of long-term variability to interannual variability. There are four possible situations at each grid cell. First, if the TWS trend is strong but the annual amplitude is small, the trend is apparent and readily noticeable. Second, if the trend is strong and the annual amplitude is large, the trend may not be apparent in the short term but may become apparent in the long term. Third, if the TWS trend is weak but the annual amplitude is large, the trend may be difficult to detect for a long time. Fourth, if the TWS trend is weak and the annual amplitude is small, the trend may be apparent and thus noticeable. In the study, if $dTWS_i$ is smaller than −100 mm and $Ratio_i$ is smaller than −1, the grid cell is defined as having an apparent drying trend. To the contrary, if $dTWS_i$ is larger than 100 mm and $Ratio_i$ is larger than 1, the grid cell is defined as having an apparent wetting trend. It turns out that the grid cells with an apparent change overlap most of those with a greater significance defined in section 3.2 (Figure 1b). Calculations of the corresponding areal fraction are described in section 3.5.

3.4. AI

AI was computed as the ratio of the 30-year (1948–1977) mean precipitation (*P*) (mm/day) to *PET* (mm/day) output by GLDAS 2.0 LIS using Noah_v3.3 (Rodell et al., 2004).

$$AI_i = \frac{P_i}{PET_i} \tag{1}$$

Following the definition of *AI* in the World Atlas of Desertification (Middleton & Thomas, 1997), we classified global land areas into different climate zones (Figure S10), with wet regions defined as where annual mean $AI \geq 0.65$ and $PET \geq 400$ mm, cold regions as where $AI \geq 0.65$ and $PET < 400$ mm, and dry regions as where $AI < 0.65$. We further subdivided dry regions into hyperarid ($AI < 0.05$), arid ($0.05 \leq AI < 0.20$), semiarid ($0.20 \leq AI < 0.50$), and dry subhumid regions ($0.50 \leq AI < 0.65$). Figure S11 presents maps of annual mean *P* and *PET* over 1948–1977, and Table S1 summarizes the climatic classification and area extent over the globe. Overlaying the two maps of TWS linear change and *AI* (Figures 1a and S10) reveals the patterns of drying and wetting in different climate zones (Figure 1d).

3.5. Area Fraction and Magnitude of TWS Linear Changes per Climatic Zone

For each land aridity type (*L*) (humid, cold, dry regions and subcategories) and associated hydrological condition (*C*) (net, positive, and negative water storage changes) we computed the fraction of total terrestrial area ($PerA^{(L,C)}$ in percentage) (excluding Antarctica and Greenland) and the expected magnitude of TWS linear changes ($M^{(L,C)}$ in millimeter) for 21 cases over the period April 2002 to January 2017. Equation 2 is used to compute the area percentage $PerA^{(L,C)}$ for aridity zone *L* with hydrological condition *C* by summing up the area of corresponding grid cells and being divided by the total land area. Equation 3 is used to compute the expected magnitude $M^{(L,C)}$ (in equivalent water depth in mm) by summing up the volumetric TWS changes of corresponding grid cells and being divided by the total area of the aridity zone *L*. The uncertainty $Uncert^{(L,C)}$ associated with the magnitude $M^{(L,C)}$ is computed as the RSS of area-weighted combined uncertainty at corresponding grid cells (Equation 4). We followed Scanlon et al. (2018) and reported the TWS change as the magnitude $M^{(L,C)}$ bounded by the uncertainty $Uncert^{(L,C)}$. In the analysis, we only include grid cells with statistically significant TWS trends defined by the number of months with consistent linear change of 9 and higher (section 3.2).

$$PerA^{(L,\,C)} = \frac{\sum_i A_i^{(L,\,C)}}{\sum_i A_i} *100\% \tag{2}$$

$$M^{(L,\,C)} = \frac{\sum_i \left[A_i^{(L,\,C)} * dTWS_i^{(L,\,C)} \right]}{\sum_i A_i^{(L)}} \tag{3}$$

$$Uncert^{(L,\,C)} = \sqrt{\frac{\sum_i \left[A_i^{(L,\,C)} * Uncert_i^{(L,\,C)2} \right]}{\sum_i A_i^{(L)}}} \tag{4}$$

3.6. Noah-MP LSM
3.6.1. Noah-MP TWS

The Noah-MP LSM (Niu et al., 2011) is an augmented multiparameterization version of the Noah LSM. The model outputs include energy, water, and carbon flux exchanges between the land surface and the atmosphere controlled by terrestrial ecohydrological processes and the corresponding storage terms. Here, we drove the Noah-MP LSM using GLDAS near-surface atmospheric forcing data (Rodell et al., 2004) and assessed the total TWS change as the sum of modeled groundwater storage, snow water equivalent, soil moisture content, canopy water storage, and plant water storage in living tissues. Consistent with postprocessing of the GRACE data, we also removed the static field averaged over all months from 2004 to 2009 from the TWS time series at each grid cell. To evaluate the uncertainties in the meteorological forcing data, we also drove the model using the Princeton forcing data (Sheffield et al., 2006).

Noah-MP explicitly represents groundwater storage in the unconfined aquifer depending on the recharge rate based on Darcy's law and the discharge rate parametrized as a function of water table depth based on the TOPMODEL concept (Niu et al., 2007). Snow water equivalent is computed as the dynamic balance of snowfall, surface deposition/sublimation and dew/evaporation, and outflow of snowmelt from the bottom of the snowpack (Niu et al., 2011). The Noah-MP LSM solves the soil moisture content using the one-dimensional Richard's equation with the Clapp-Hornberger soil water retention model (Clapp & Hornberger, 1978). The temporal evolution of canopy water storage is calculated as the sum of snowfall, rainfall, dew, and deposition minus the sum of drip, evaporation, sublimation, and throughfall. The current version of Noah-MP also explicitly represents the plant water storage as the residual of root water uptake and transpiration (Niu et al., 2020; Wang et al., 2018). Although the plant water storage may be negligible compared to other water storages, it is critical for plants' stomatal opening and transpiration.

3.6.2. Noah-MP Updates and Parameterization Options Used in Simulations

The Noah-MP version used in this study explicitly represents plant water storage supplied by dynamic root water uptake through hydrotropic root growth to meet the transpiration demand (Niu et al., 2020). The dynamic vegetation submodel (Dickinson et al., 1998) predicts leaf area index, which is converted from the leaf carbon mass as the residual of photosynthates translocated to leaf and leaf turnover, respiration, and death. Plant transpiration water loss is controlled by stomatal resistance, which is regulated by the plant water storage, air temperature, humidity, CO_2 concentration, light, and the leaf boundary layer resistance. In the current version, the plant water availability factor β controlling the stomatal resistance is parameterized as a function of water storage in the living plant tissues, M_q (Niu et al., 2020).

$$\beta = min\left(1.0, \frac{M_q - M_{q,\,wilt}}{M_{q,\,max} - M_{q,\,wilt}}\right) \tag{5}$$

where $M_{q,wilt}$ represents the minimum plant water storage at the wilting point of 30 bars (306 m or 3.0 MPa) and $M_{q,max}$ the maximum plant water storage when the plants are at full hydration. Actually, this β represents the plant water available for transpiration ($M_q - M_{q,wilt}$) relative to the maximum water that a plant can lose through transpiration until its wilting point ($M_{q,max} - M_{q,wilt}$). A low β indicates that the plants are under water stress due to limited water storage and restricts the opening of stomata, reducing CO_2 uptake and carboxylation and transpiration water loss. While transpiration depletes the plant water storage, M_q is replenished by root water uptake driven by the water pressure gradient between the soils and the roots and computed analogous to Ohm's law (see Niu et al., 2020, for details). This new version of Noah-MP largely enhances the ecosystem resilience to water stress over drylands and during droughts, while its previous version and other LSMs are generally more vulnerable to water stress, producing lower leaf area index or ecosystem productivity during droughts (e.g., Mao et al., 2013; Zhu et al., 2019).

Noah-MP explicitly represents the groundwater storage in unconfined aquifers or "buckets" below its shallow, 2-m soil column, which receive recharging water during wet periods to "buffer" water stress that the plants may experience in later droughts through upward flows driven by capillary forces exerted by the soil matrix. Noah-MP modified the suction head of soil matrix with a micropore volume fraction (f_{mic}; Niu et al., 2011) due to the common presence of macropores in soils formed by soil aggregates, fissures, dead roots, and worm holes (Beven & Germann, 1982), which would reduce the suction head in a linear way. As the value of f_{mic}, which ranges from 0.0 to 1.0, approaches 0.0, the lower boundary becomes a free drainage boundary condition, while $f_{mic} = 1.0$ represents a full effect of capillary rise of groundwater. In this study, we used a constant f_{mic} value of 0.8 over global continents for lack of data.

We applied the Monin-Obukhov similarity theory to compute the exchange coefficients of sensible and latent heat within the surface layer (Brutsaert, 1982). For supercooled liquid water option, we used a general form of freezing point equation, which requires no iteration (Niu & Yang, 2006). In terms of soil permeability, we assumed that frozen soils exert linear effects on soil hydraulic conductivity and diffusivity, depending on total soil moisture and impermeable fraction due to frozen soils (Niu & Yang, 2006). We adopted the modified scheme of two-stream radiation transfer through the plant canopy (Niu & Yang, 2004) and the CLASS-type for snow surface albedo (Verseghy, 1991). Partitioning of precipitation into rainfall and snowfall uses a sigmoidal relationship of the wet bulb temperature (Wang et al., 2019). The lower boundary condition
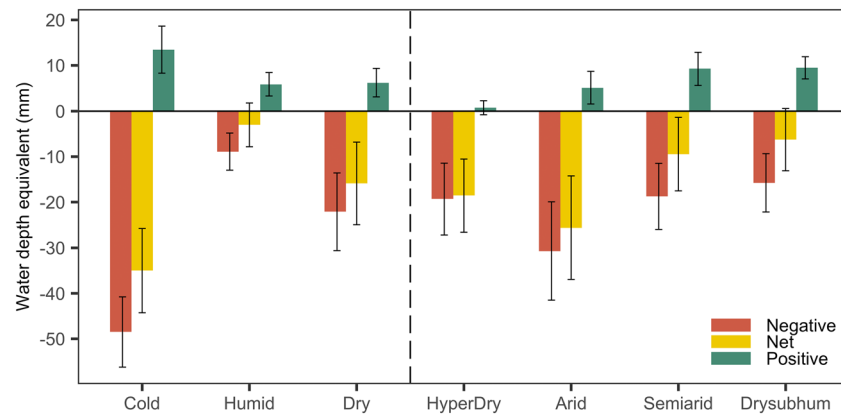
Figure 2. TWS linear change from April 2002 to January 2017 over cold, humid, and dry regions (left) and the subcategories of dry climate (right). The error bars represent uncertainty $Uncert^{(L,C)}$. Only grid cells with statistically significant TWS trends are included.

of soil temperature at 8 m deep is assumed the hourly climatology of the near-surface air temperature. We used a semi-implicit snow/soil temperature time scheme. Table S2 summarizes the options we adopted in this study.

3.6.3. Noah-MP Parameters Used in Simulations

The dominant vegetation types covering these three regions are shrubland (PFT 8) and grassland (PFT 7). The dominant soil types are loam (SOIL 6) and clay loam (SOIL 9). In Tables S3 and S4, we list the key parameters for the dominant vegetation types and soil types, respectively. In the supporting information, we include an explanation and grid cell number of each vegetation and soil type over the drylands in the southwestern North America, the Middle East, and North China (Tables S5 and S6).

4. Results

4.1. GRACE TWS Changes

4.1.1. Dryland Regions

The TWS linear change exhibits a roughly latitudinal pattern that is particularly pronounced over midlatitude subtropical dry regions (Figures 1a and 1d). During the period of analysis, negative trends were found for the dry regions over the southwestern North America, northern Sahara, the Middle East, and North China in the NH and western Australia, central Argentina, and the Patagonia plateau in the Southern Hemisphere. Importantly, the higher degree of statistical significance and change-to-amplitude ratios in these regions indicate that their TWS linear changes are more significant (Figure 1b) and apparent (Figure 1c). In contrast, dry regions at the southern tip of Africa and the wet-to-dry transitional (dry subhumid) region of Australia became wetter (Figure 1d), with smaller absolute values of change-to-amplitude ratios and lower degree of statistical significance.

Overall, the "dry lost water" land area accounts for 7.9% of the global land area, while the "dry gained water" area is smaller (~3.1%). In terms of water depth, dry regions experienced a net global water loss of 15.9 ± 9.1 mm (Figure 2), with 22.1 ± 8.5 mm loss occurring in the "dry lost water" regions partially offset by 6.2 ± 3.1 mm gain in the "dry gained water" regions. The TWS changes in the "dry lost water" regions are more significant and apparent than the "dry gained water" regions (Figures 1b and 1c), indicating a stronger drying than wetting signals over global drylands.

These large-scale subtropical drying patterns may be related to strengthening of the descending branch of the Hadley cell under global warming (Lau & Kim, 2015; Trenberth, 2011), the drying tendency of continents due to enhanced land warming (Byrne & O'Gorman, 2015), and anthropogenic influences through groundwater extraction and agricultural irrigation (Gleeson et al., 2012; Reager et al., 2016; Rodell et al., 2018). However, the trends may be temporary due to the influence of large-scale atmospheric oscillations (Eicker et al., 2016; Phillips et al., 2012; Rodell et al., 2018). The dryland regions in the central Australia show relatively strong negative correlations between TWS time series and multivariate ENSO index (Figure S14). Also,

spurious signals associated with postprocessing of the GRACE data may also influence trend estimates in affected regions, such as northwestern China (Humphrey et al., 2016).

Closer inspection of the dry climate region subcategories (Figure 2) reveals that decreases in TWS occurred mainly in hyperdry and arid regions, with net water losses of 18.6 ± 8.0 and 25.6 ± 11.4 mm, respectively. Meanwhile, water storage changes in semiarid regions (-9.4 ± 8.1 mm) and transitional dry subhumid zones (-6.3 ± 6.8 mm) were uncertain.

4.1.2. Humid Regions

Over wet tropical regions, where convective storms dominate, the Amazon gained water, whereas the central Congo and Southeast Asia lost water (Figures 1a and 1d). It is known that precipitation over tropical land has decreased by ~0.3% per decade in a warming climate, explained by a negative relationship between precipitation and temperature anomalies (Gu et al., 2007; Liu et al., 2012). The correlation coefficients between TWS and ENSO and PDO indexes are high over Southeast Asia (Figures S14 and S15), possibly indicating an influence of natural climate variability on land water storage. However, the TWS linear change over these regions is not apparent (Figure 1c) and the associated degree of statistical significance is low (Figure 1b). Wet subtropical monsoon regions, including southwestern African Plateau and southern China, became wetter (Figures 1a and 1d), possibly due to global intensification of the monsoons (B. Wang et al., 2012). Wet extratropical regions in the NH (north of the subtropics and the southern part of the cold regions), where frontal storms dominate, became wetter—with the wetting trend being most pronounced over North America. This may be caused by changes in precipitation patterns due to poleward shifts of storm tracks (Trenberth, 2011; Yin, 2005) and decreases in evaporation caused by tree mortality under a warming climate (Allen et al., 2010). However, other factors, such as tectonics, may also affect GRACE measurements (Cooley & Landerer, 2019). Earthquakes in Hokkaido in 2003, Sumatra-Andaman in 2004, and Tohoku-Oki in 2011 were found to introduce anomalies of geoid height in the vicinity of epicenters during the events (De Viron et al., 2008; Junyan et al., 2015; Sun & Zhou, 2012; L. Wang, Shum, et al., 2012). These anomalies in the local time series might introduce outliers when calculating TWS trends.

Overall, the land area corresponding to "humid gained water" accounts for 2.3% of the global land area, while that corresponding to "humid lost water" is smaller (~2.2%). In terms of water depth, wet regions experienced a net global water change of 3.0 ± 4.8 mm (Figure 2), with 5.9 ± 2.5 mm of gain offset by 8.9 ± 4.1 mm of loss. Therefore, the pattern of drying and wetting over global humid regions are inconclusive when accounting for the relatively large uncertainty. TWS changes over humid regions are not as significant and apparent as changes over dryland regions (Figures 1b and 1c).

4.1.3. Cold Regions

In the NH high-latitude cold regions, the land area that experienced wetting accounts for ~1.9% of global land area and is smaller than the area that lost water (~2.8%). Overall, these cold regions experienced net water loss of 35.0 ± 9.3 mm (Figure 2), with the 13.5 ± 5.2 mm gain in "cold gained water" regions offset by the 48.5 ± 7.7 mm loss in "cold lost water" regions. The water loss events mainly occurred in North America, with almost all months passing the significance test and the negative TWS changes are apparent. This amount of loss may result from melting of snow and ice due to the warming climate (IPCC, 2014).

4.2. Data Analysis and Model Simulations Over Three Selected Dryland-Drying Regions

As the GRACE satellites record the combined natural and anthropogenic effects on TWS changes, isolating the individual contributions to the trends is challenging. To understand the likely major causes of the observed TWS negative trends over dryland regions, we conducted climatic data analysis and model simulations over three selected dryland regions (Figure 3a) located in the southwestern North America (Region 1), the Middle East (Region 2), and North China (Region 3) that show the most apparent and significant decreasing trends. Figures 3b–3g show the effects of atmospheric demand (PET) and supply (P) on the TWS trends. Annual AI is computed as the ratio of annual P to annual PET from 1948 to 2016. The correlation coefficients between annual P and PET with ENSO and PDO indexes over 2002 to 2016 are provided to evaluate impacts of natural climate variability (Table 1). Besides the atmospheric control, we also ran virtual experiments with the Noah-MP LSM to investigate effects of terrestrial ecohydrological processes on TWS variations. Figure 4 compares the GRACE TWS anomaly and Noah-MP simulated TWS anomaly over the three regions. Figure 5 shows cumulative deviations (Shuttleworth, 2012) of the model-simulated fluxes, that is, accumulated departures in monthly water fluxes from their mean values during GRACE period. The
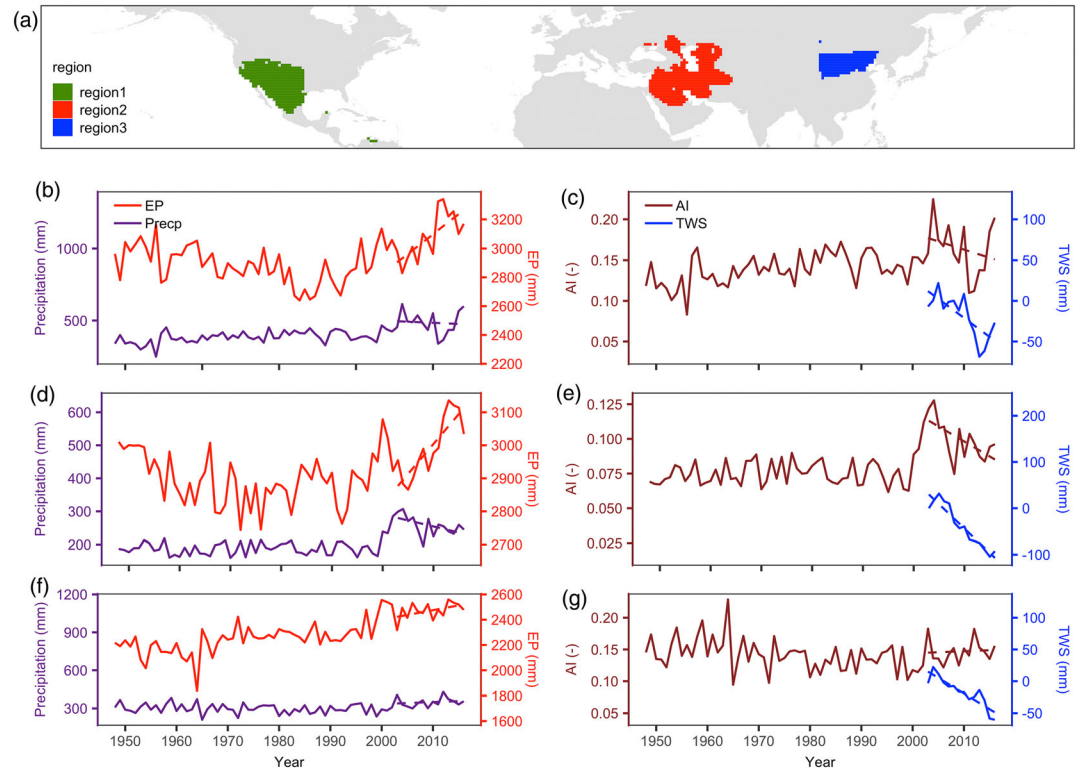
Figure 3. (a) Locations of three dryland-drying regions in Northern Hemisphere midlatitudes used in Noah-MP LSM simulations. Regions 1, 2, and 3 are located in the southwestern North America, the Middle East, and North China. Time series of annual total *PET* (EP in the legend) and precipitation (Precp), annual aridity index (*AI*), and annual mean TWS for the three dryland-drying regions (b, c) southwestern North America, (d, e) Middle East, and (f, g) North China from 1948 to 2016.

advantage of using cumulative deviation is that it can amplify the signals of drying and wetting trends. Besides the control model experiment (CTRL with f_{mic} at 0.8 and the dynamic root scheme described in section 3.6), we also conducted two additional model sensitivity experiments FMIC (f_{mic} at 0.2 and dynamic root described in section 3.6) and ROOT (f_{mic} at 0.8 and a prescribed, static root profile) to understand TWS responses to groundwater and root dynamics over the dryland regions.

Over the drylands in the southwestern North America and the Middle East, *PET* has experienced an increasing trend since the 1980s (Figures 3b and 3d), implying an enhanced atmospheric demand for water vapor caused by the warming, whereas the atmospheric supply (*P*) declined during the GRACE period. TWS trends closely follow the declining *AI* (Figures 3c and 3e), indicating a control of the atmospheric supply-and-demand contrast on TWS under the warming over the two regions. TWS lags approximately 1 year behind *AI*, possibly due to a delayed response of the TWS to climatic variations. The correlation coefficients between annual *PET* with ENSO and PDO indexes are relatively small over the two regions (Table 1). However, the coefficients between the indexes with *P* are larger, indicating possible influences of natural climate variability on direct water input from the atmosphere to the land surface.

Table 1
Correlation Coefficients Between Annual Mean PET and P With Multivariate ENSO and PDO Indexes From 2002 to 2017

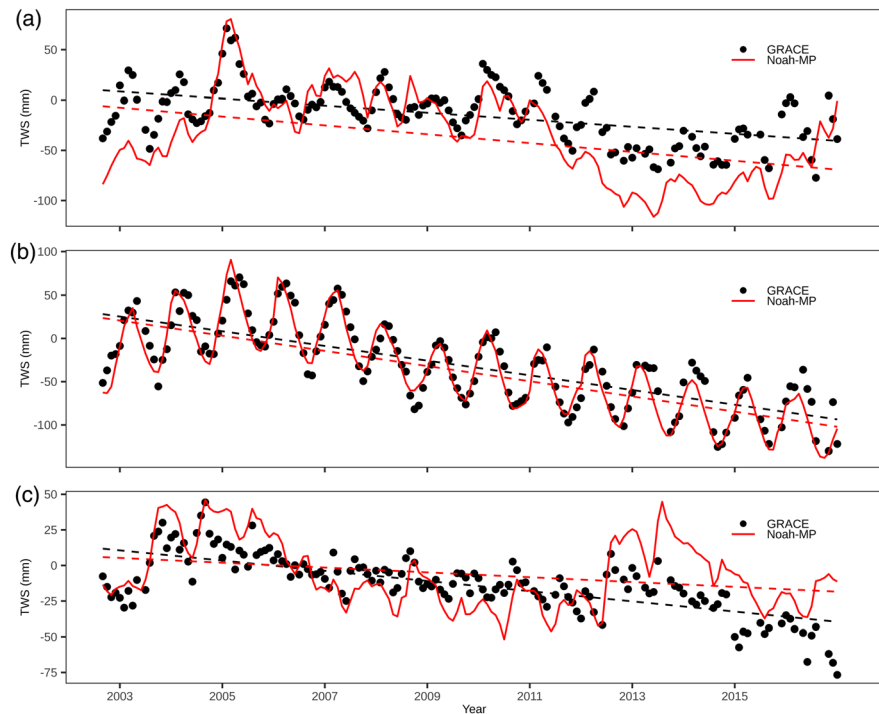|	ENSO with *P*	PDO with *P*	ENSO with *PET*	PDO with *PET*
Region 1	0.42	0.56	−0.19	−0.24
Region 2	0.49	0.30	0.09	0.12
Region 3	−0.18	−0.11	0.22	0.03

Figure 4. Monthly TWS anomalies by GRACE data and the Noah-MP model simulations over (a) the southwestern North America, (b) the Middle East, and (c) North China from April 2002 to January 2017. The dashed lines represent least squares linear trends. Over the southwestern North America, the trend values are −0.29 and −0.38 mm/month using GRACE data and Noah-MP model outputs, respectively. Over the Middle East, the trend values are −0.71 and −0.72 mm/month. Over North China, the trend values are −0.30 and −0.15 mm/month.

The model-simulated TWS follows the observed decreasing tendency and variability over the two regions (Figure 4). Cumulative deviations of the water fluxes between the land surface and the atmosphere (Figure 5) show that precipitation supply plays a dominant role in controlling TWS than actual *ET*. Contrary to the increasing atmospheric demand *PET*, the actual *ET* is largely suppressed by the limited land water supply in the dry regions. The model-simulated TWS slightly overestimates the negative trend (−0.38 mm/month) of the GRACE estimates (−0.29 mm/month) over the southwestern North America (Figure 4a). This overestimation of the negative TWS trend is mainly due to an underestimation of TWS anomalies after the drought since 2011 (Long et al., 2013). Additional experiments indicate that the modeled TWS anomalies are sensitive to different values of the micropore volume fraction, f_{mic}, and different schemes of plant hydraulics and root dynamics (Figure 6). The deeper trough of the modeled TWS anomaly since 2011 may be caused by overestimation in the capillary rise of groundwater (too large f_{mic}) or too strong plant root water uptake (Figure 6a). With the same f_{mic} value and plant hydraulics, the model (CTRL) produces the TWS trend (−0.72 mm/month) that agrees fairly well with the GRACE TWS trend (−0.71 mm/month) and seasonal variability (Figure 4b) over the drylands in the Middle East. Without implementing human water withdrawal in the model, Noah-MP driven by the GLDAS atmospheric forcing data simulates the decreasing trends of TWS. Based on the climatic data analyses (Figure 3), and supported by the modeling results (Figure 4), we infer that climatic factors played a dominant role in causing the declining TWS trends over the southwestern North America and the Middle East than human water withdrawal.

However, over the GRACE period, the GRACE TWS trend is not consistent with the *AI* trend in North China (Figure 3g). While the increasing *AI* indicates a slightly wetting tendency under the warming conditions (Figures 3g and 3f), the GRACE TWS indicates a decreasing trend (−0.30 mm/month). The correlation coefficients between *P* and *PET* with ENSO and PDO indexes are relatively low, with absolute values smaller than 0.4 (Table 1). Further, the modeled TWS trend (−0.15 mm/month) explains only about one half of the trend detected by GRACE (Figure 4c). The underestimation of the negative trend by Noah-MP from 2012 on indicates that climatic forcing cannot completely explain the TWS decreasing trend detected by
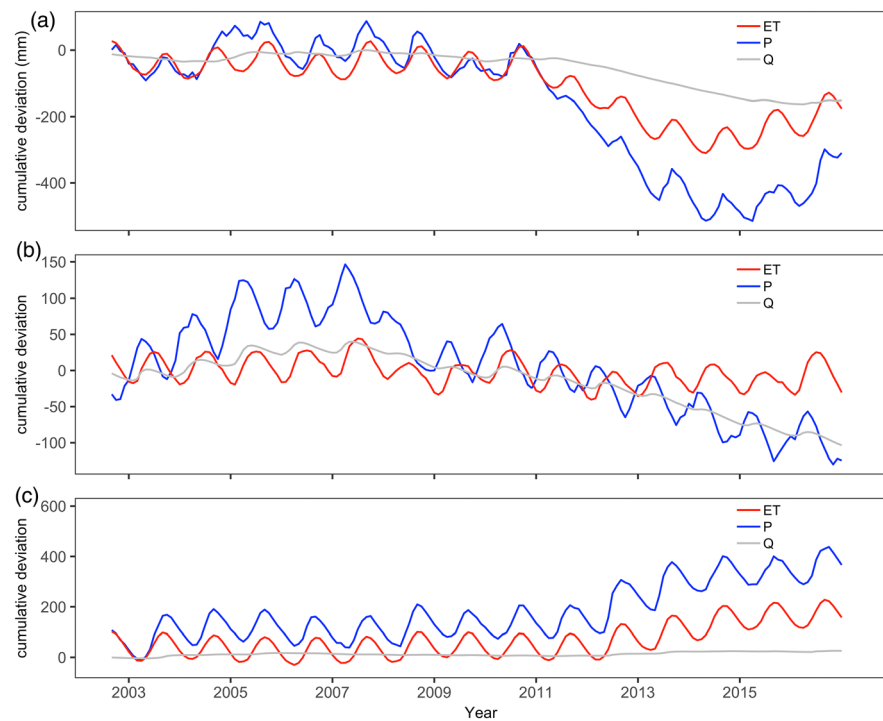
Figure 5. Cumulative deviations of monthly evapotranspiration (*ET*), precipitation (*P*), and runoff (*Q*) over (a) the southwestern North America, (b) the Middle East, and (c) North China from April 2002 to January 2017. *ET* and *Q* are simulated by the Noah-MP LSM, and *P* is calculated using the GLDAS forcing data. Cumulative deviations are computed as accumulated departures in monthly water fluxes from their mean values.

GRACE. It is likely, therefore, that human activities (Yuan et al., 2019), such as groundwater withdrawal for irrigation may be the dominant factor; this interpretation is supported by the map of fractional irrigation area (Figure S20). Xu et al. (2019) also found the underestimation of the TWS change relative to GRACE over North China using two global hydrological models. However, after accounting for human water use, their modeled TWS trend is comparable to the GRACE observation. Besides human impacts, our additional virtual experiments indicate that the simulations are sensitive to the representations of the terrestrial ecohydrological processes (Figure 6).

The current version of Noah-MP explicitly represents groundwater dynamics and plant water storage dynamics through root water uptake, which is proportional to root surface area at different soil layers that are converted from the root biomass by specific root surface area. The model allows more photosynthate translocation to roots when the plants are under water stress and represents root hydrotropism through more translocation of photosynthate to but less turnover of root biomass in wetter soil layers. These developments enable a substantial advancement in representation of ecosystem function and resilience to water stress. Our sensitivity experiments indicate that the Noah-MP LSM conserves water mass, and the modeled water fluxes and TWS anomalies are sensitive to different values of micropore volume fraction, f_{mic}, and different schemes of plant hydraulics and root dynamics (Table 2). While the overall "dryland-drying" trends remain very similar, the TWS trends from these experiments differ to some extent, suggesting the importance of terrestrial water "supply" under the warming-caused increase in water "demand." In CTRL, Noah-MP uses the same model parameters (e.g., $f_{mic} = 0.8$) for all the three regions. This may lead to overestimation of the negative trend over the southwestern North America, while the model matches well with the GRACE trend and variability over the Middle East.

Given the observational facts of widespread woody encroachment (Andela et al., 2013), dryland greening (Fensholt et al., 2012; Zhu et al., 2016), and increasing trends in the net carbon sink in semiarid regions (Ahlström et al., 2015) despite warming-associated drying trend, dryland ecosystems may have become an "active" driving force for TWS by "pumping" deeper soil water and groundwater through extended
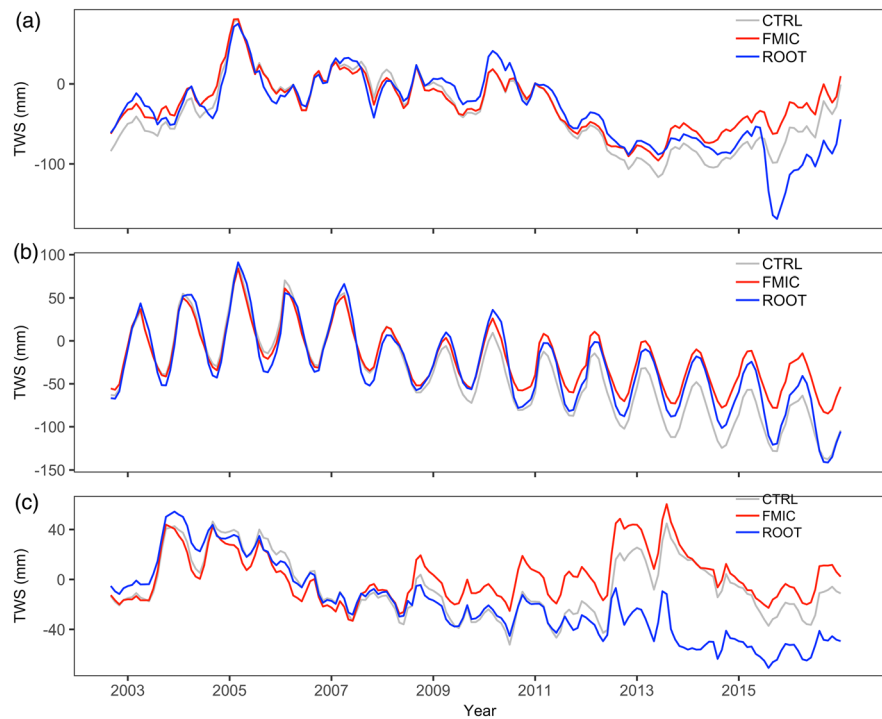
Figure 6. Modeled monthly TWS anomalies over (a) the southwestern North America, (b) the Middle East, and (c) North China from April 2002 to January 2017 by CTRL, FMIC, and ROOT experiments. CTRL implements the dynamic root scheme (section 3.6) with f_{mic} at 0.8. FMIC implements the dynamic root scheme with f_{mic} at 0.2. ROOT uses a prescribed, static root scheme with f_{mic} at 0.8.

rooting systems that enable plants to survive droughts (Fan et al., 2017). Compared to other ecosystems, dryland ecosystems show much stronger resiliency or higher capacity to tolerate water stress. The rain use efficiency (or biomass productivity per unit rainfall) of dryland ecosystems tends to increase under drier conditions and converge across biomes to a common maximum value during the driest conditions (Huxman et al., 2004; Ponce-Campos et al., 2013).

Based on the climatic data analyses and model simulations, we infer that the dryland-drying patterns are largely controlled by the climatic demand-and-supply contrast that is strongly regulated by terrestrial ecohydrological processes and human water withdrawal. Over the drylands in the southwestern North America and the Middle East, climatic factors play a dominant role. However, comparable effects of climatic factors and anthropogenic interventions may determine the negative TWS change over North China. This interpretation is consistent with a recent analysis using partial least squares regression (Yuan et al., 2019).

5. Discussion

Overall, our GRACE TWS data analysis indicates that the "dry lost water" land area is larger than that of "dry gained water," while the "humid gained water" land area is larger than that of "humid lost water."

Table 2
Averaged Water Budgets of P, ET, and Runoff, Q (mm/Month), Over Region 1 (Southwestern North America), Region 2 (the Middle East), and Region 3 (North China) From April 2002 to January 2017 by CTRL, FMIC, and ROOT Experiments

	Region 1			Region 2			Region 3		
Experiment	*P*	*ET*	*Q*	*P*	*ET*	*Q*	*P*	*ET*	*Q*
CTRL	39.0	34.8	3.8	20.6	18.2	2.8	28.5	27.3	1.2
FMIC	39.0	32.2	6.4	20.6	16.3	4.6	28.5	25.4	3.0
ROOT	39.0	31.1	3.4	20.6	17.0	1.7	28.5	25.6	0.7

Dry regions experienced a net water loss of 15.9 ± 9.1 mm, while wet regions experienced a net water change of 3.0 ± 4.8 mm. These findings support the amplification of the contrast between dry and wet patterns over land, in particular the signal of water storage declining in drylands. However, the apparentness map and the statistical significance map indicate that, over tropical wet regions, the signal is less obvious (shows less contrast) and less significant, whereas the signal over subtropical midlatitude "dry lost water" regions is more apparent and significant. Drying dry regions exhibit a change-to-amplitude ratio exceeding 1 (Figure S9) and the number of months with significant TWS trends exceeding 9. Overall, we conclude that water storage declined over drylands, supported by TWS data at the decadal scale.

We also supported the "dryland-drying" hypothesis using the CSR GRACE mascons (Figures S12 and S13). The spatial patterns of drying/wetting over climate regions, the apparentness and statistical significance of TWS changes, are comparable to those using SH solutions. Results from both SH and mascons indicate a greater areal extent of dryland-drying areas than dryland-wetting areas (Figure S12) and a net negative change of water amount over global dryland regions (Figure S13). However, despite the comparable large-scale spatial patterns, there are disparities between values of TWS changes and regional-scale patterns on the maps. The magnitude of TWS changes estimated using the GRACE mascons from CSR is larger than that using SH (Figure S12a). The difference has been demonstrated in previous research by Scanlon et al. (2016). Unlike SH, CSR mascons exhibit bipolar patterns over drying regions in the SW North America and East Brazil, possibly due to a higher spatial resolution at 0.5° and different algorithms.

Most current fully coupled climate models, however, are unable to simulate the "dryland-drying" trends (Kumar et al., 2015). This may be because the modeled ET cannot exceed precipitation at decadal scales due to limited availability of water over dry regions, whereas over the oceans, the water availability is effectively unlimited (Kumar et al., 2015). Also, the current macroscale hydrological models and uncoupled LSMs for use in the climate models are unable to generate accurate estimates of ET (especially its accumulative effects on TWS) and produce much weaker TWS trends compared to that of GRACE (Scanlon et al., 2018) due to incomplete representations of the ecohydrological processes controlling ET, for example, plant hydraulics and root dynamics. In addition, enhanced groundwater loss through vaporization and diffusion within the soil and evaporation at the soil surface under a warming climate, though at a small rate, may not be negligible at decadal scales (Kamai & Assouline, 2018). It is most likely that through these "pumping" mechanisms, ET becomes larger than precipitation at decadal scales, causing the "dryland-drying" trends.

In this study, our simulated TWS using the Noah-MP LSM can closely follow the GRACE observations and produce comparable trends over drylands in the southwestern North America and Middle East. To test model consistency and the sensitivity of Noah-MP to different meteorological forcing data, we repeated the CTRL experiment using the Princeton reanalysis data (Sheffield et al., 2006). The TWS trends and seasonal variations are very similar using the different climate forcing data (Figure S16). However, the Princeton forcings produce higher TWS anomalies before 2005 and smaller annual amplitudes throughout the GRACE period than the GLDAS forcings. Starting 2001, monthly precipitation of GLDAS exceeds that of the Princeton reanalysis, in particular during wet seasons (Figure S17). However, the atmosphere is less humid (QAIR) represented by GLDAS than the Princeton data (Figure S19). Therefore, the model is driven by both greater water supply and greater demand using GLDAS forcings than Princeton reanalysis data. The atmospheric supply-demand balance and its cumulative effects over time lead to the discrepancies in the temporal variations of simulated TWS by the two forcing data sets. Despite the differences, experiments with both climatic forcing data sets support the "dryland-drying" conclusion with negative TWS changes.

Uncertainties in model structure and parameters may substantially affect the TWS modeling results as reflected from the model sensitivity experiments (Figure 6) and thus confound disaggregation of the climatic and anthropogenic drivers. The model version used in the CTRL experiment largely improves the model realism with augmentations in representing plant hydraulics and root dynamics, although it is still uncertain in representing the soil water retention characteristics by different models (Niu et al., 2020). Our conclusion that anthropogenic water withdrawal may have played a more dominant role in the declining TWS in Northern China based on the modeling results is further confirmed by the map of fractional irrigation area (Figure S20) and consistent with a recent analysis using partial least squares regression (Yuan et al., 2019). In this study, we used the Noah-MP LSM as an interpreting tool to explore possible causes to the dryland drying trend that needs ET to be greater than precipitation at decadal scales. However, to more accurately discern

the two drivers, it requires further advancements in both model developments based on improved predictive understanding of the terrestrial ecohydrological processes and data developments based on in situ metered water use data and remote sensing data (e.g., the irrigated area).

6. Conclusions

Our analysis of the GRACE TWS suggests that more than half of the global drylands (58%) experienced negative TWS changes during the period April 2002 to January 2017. Dry regions lost ~15.9 ± 9.1 mm of water, with 22.1 ± 8.5 mm loss occurring in the "dry lost water" regions partially offset by 6.2 ± 3.1 mm gain in the "dry gained water" regions. Decreases in TWS occurred mainly in hyperdry (18.6 ± 8.0 mm) and arid regions (25.6 ± 11.4 mm). The TWS changes over the "dry lost water" regions show a higher degree of statistical significance than over the "dry gained water" regions. Compared to local annual amplitudes of variability, the TWS changes were more apparent in dry regions than in wet regions, highlighting a drying signal from drylands. However, due to the brevity of the 15-year GRACE period, the TWS trends may be subject to interannual and interdecadal hydrological variability.

To understand the large-scale dryland-drying mechanisms over the NH midlatitudes, we used the near-surface climate data sets from GLDAS and model simulations conducted using the Noah-MP LSM. Over drylands in the southwestern North America and the Middle East, the climate data and GRACE TWS consistently indicate a drying signal. Model simulations without anthropogenic impacts suggest that the negative TWS trends are largely attributable to climate drivers regulated by terrestrial ecohydrological processes over the two regions. However, over the drylands in North China, the GRACE TWS anomaly data indicate a drying trend while the climate data suggest a slightly wetting trend. In addition, the model simulations driven only by climatic forcings are not able to reproduce the observed TWS trend. The climate data analyses and model simulations suggest that the drying trends in North China may be largely attributed to intense anthropogenic water withdrawals as supported by the large areal extent of irrigated agricultural lands over North China. Overall, our data analysis and model simulations suggest that climatic factors plays a more dominant role in the declining water storage at a decadal scale over the drylands in the southwestern North America and the Middle East than does the anthropogenic water withdrawal, while anthropogenic groundwater pumping is more dominant in North China.

Conflict of Interest

The authors declare no competing financial interests.

Data Availability Statement

GRACE land data are available online (https://grace.jpl.nasa.gov), supported by the NASA MEaSUREs Program. GRACE GRCTellus Land grids can be downloaded online (https://grace.jpl.nasa.gov/data/get-data/monthly-mass-grids-land/). CSR mascon TWS data can be downloaded online (http://www2.csr.utexas.edu/grace/RL05_mascons.html). Contemporary rates of GIA corrections are available for download from the GRACE website (https://podaac-tools.jpl.nasa.gov/drive/files/GeodeticsGravity/tellus/L3/gia/1-deg). Percentage of irrigation areas can be found on Food and Agricultural Organization (FAO) website (http://www.fao.org/nr/water/aquastat/irrigationmap/index10.stm). Multivariate ENSO index data can be downloaded online (https://www.esrl.noaa.gov/psd/enso/mei/). PDO index can be found online (http://research.jisao.washington.edu/pdo/PDO.latest.txt). GLDAS data are available for download online (https://disc.gsfc.nasa.gov/datasets?keywords=GLDAS&page=1&source=Models%2FAnalyses%20Noah-LSM&temporalResolution=3%20hours&spatialResolution=1%20%C2%B0%20x%201%20%C2%B0).

References

Ahlström, A., Raupach, M. R., Schurgers, G., Smith, B., Arneth, A., Jung, M., et al. (2015). The dominant role of semi-arid ecosystems in the trend and variability of the land CO_2 sink. *Science*, *348*, 895–899. https://doi.org/10.1126/science.aaa1668

Allen, C. D., Macalady, A. K., Chenchouni, H., Bachelet, D., McDowell, N., Vennetier, M., et al. (2010). A global overview of drought and heat-induced tree mortality reveals emerging climate change risks for forests. *Forest Ecology and Management*, *259*(4), 660–684. https://doi.org/10.1016/j.foreco.2009.09.001

Allen, M. R., & Ingram, W. J. (2002). Constraints on future changes in climate and the hydrologic cycle. *Nature*, *419*(6903), 224–232. https://doi.org/10.1038/nature01092

Andela, N., Liu, Y. Y., van Dijk, I. J. M., de Jeu, R. A. M., & McVicar, T. R. (2013). Global changes in dryland vegetation dynamics (1988–2008) assessed by satellite remote sensing: Comparing a new passive microwave vegetation density record with reflective greenness data. https://doi.org/10.5194/bg-10-6657-2013

Beven, K., & Germann, P. (1982). Macropores and water flow in soils. *Water Resources Research*, *18*(5), 1311–1325. https://doi.org/10.1029/WR018i005p01311

Brutsaert, W. (1982). Evaporation into the atmosphere: Theory, history and applications, 1.

Byrne, M. P., & O'Gorman, P. A. (2015). The response of precipitation minus evapotranspiration to climate warming: Why the "wet-get-wetter, dry-get-drier" scaling does not hold over land. *Journal of Climate*, *28*, 8078–8092. https://doi.org/10.1175/JCLI-D-15-0369.1

Caron, L., Ivins, E. R., Larour, E., Adhikari, S., Nilsson, J., & Blewitt, G. (2018). GIA model statistics for GRACE hydrology, cryosphere and ocean science. *Geophysical Research Letters*, *45*, 2203–2212. https://doi.org/10.1002/2017GL076644

Castellazzi, P., Martel, R., Rivera, A., Huang, J., Pavlic, G., Calderhead, A. I., et al. (2016). Groundwater depletion in Central Mexico: Use of GRACE and InSAR to support water resources management. *Water Resources Research*, *52*, 5985–6003. https://doi.org/10.1002/2015WR018211

Chen, J. L., Wilson, C. R., Blankenship, D., & Tapley, B. D. (2009). Accelerated Antarctic ice loss from satellite gravity measurements. *Nature Geoscience*, *2*(12), 859–862. https://doi.org/10.1038/ngeo694

Chou, C., Neelin, J. D., Chen, C.-A., & Tu, J.-Y. (2009). Evaluating the "rich-get-richer" mechanism in tropical precipitation change under global warming. *Journal of Climate*, *22*(8), 1982–2005. https://doi.org/10.1175/2008JCLI2471.1

Clapp, R. B., & Hornberger, G. M. (1978). Empirical equations for some soil hydraulic properties. *Water Resources Research*, *14*(4), 601–604. https://doi.org/10.1029/wr014i004p00601

Cleveland, R. B., Cleveland, W. S., McRae, J. E., & Terpenning, I. (1990). STL: A seasonal-trend decomposition procedure based on loess. *Journal of Official Statistics*, *6*(1), 3–73.

Cooley, S. S., & Landerer, F. W. (2019). Gravity Recovery and Climate Experiment Follow-on (GRACE-FO) Level-3 data product user handbook (Jet Propulsion Laboratory California Institute of Technology).

De Viron, O., Panet, I., Mikhailov, V., Van Camp, M., & Diament, M. (2008). Retrieving earthquake signature in grace gravity solutions. *Geophysical Journal International*, *174*(1), 14–20. https://doi.org/10.1111/j.1365-246X.2008.03807.x

Delgado-Baquerizo, M., Maestre, F. T., Gallardo, A., Bowker, M. A., Wallenstein, M. D., Quero, J. L., et al. (2013). Decoupling of soil nutrient cycles as a function of aridity in global drylands. *Nature*, *502*, 672–676. https://doi.org/10.1038/nature12670

Dickinson, R. E., Shaikh, M., Bryant, R., & Graumlich, L. (1998). Interactive canopies for a climate model. *Journal of Climate*, *11*, 2823–2836. https://doi.org/10.1175/1520-0442(1998)011<2823:ICFACM>2.0.CO;2

Du, J., Kimball, J. S., Velicogna, I., Zhao, M., Jones, L. A., Watts, J. D., & Kim, Y. (2019). Multi-component satellite assessment of drought severity in the contiguous United States from 2002 to 2017 using AMSR-E and AMSR2. *Water Resources Research*, *55*, 5394–5412. https://doi.org/10.1029/2018WR024633

Eicker, A., Forootan, E., Springer, A., Longuevergne, L., & Kusche, J. (2016). Does GRACE see the terrestrial water cycle "intensifying"? *Journal of Geophysical Research: Atmospheres*, *121*, 733–745. https://doi.org/10.1002/2015JD023808

Famiglietti, J. S. (2014). The global groundwater crisis. *Nature Climate Change*, *4*, 945–948. https://doi.org/10.1038/nclimate2425

Famiglietti, J. S., Lo, M., Ho, S. L., Bethune, J., Anderson, K. J., Syed, T. H., et al. (2011). Satellites measure recent rates of groundwater depletion in California's Central Valley. *Geophysical Research Letters*, *38*, L03403. https://doi.org/10.1029/2010GL046442

Famiglietti, J. S., & Rodell, M. (2013). Water in the balance. *Science*, *340*, 1300–1130. https://doi.org/10.1126/science.1236460

Fan, Y., Miguez-Macho, G., Jobbágy, E. G., Jackson, R. B., & Otero-Casal, C. (2017). Hydrologic regulation of plant rooting depth. *Proceedings of the National Academy of Sciences*, *114*, 10,572–10,577. https://doi.org/10.1073/pnas.1712381114

Feng, W., Zhong, M., Lemoine, J.-M., Biancale, R., Hsu, H.-T., & Xia, J. (2013). Evaluation of groundwater depletion in North China using the Gravity Recovery and Climate Experiment (GRACE) data and ground-based measurements. *Water Resources Research*, *49*, 2110–2118. https://doi.org/10.1002/wrcr.20192

Fensholt, R., Langanke, T., Rasmussen, K., Reenberg, A., Prince, S. D., Tucker, C., et al. (2012). Greenness in semi-arid areas across the globe 1981–2007—An Earth Observing Satellite based analysis of trends and drivers. *Remote Sensing of Environment*, *121*, 144–158. https://doi.org/10.1016/j.rse.2012.01.017

Forootan, E., Safari, A., Mostafaie, A., Schumacher, M., Delavar, M., & Awange, J. L. (2017). Large-scale total water storage and water flux changes over the arid and semiarid parts of the Middle East from GRACE and reanalysis products. *Surveys in Geophysics*, *38*, 591–615. https://doi.org/10.1007/s10712-016-9403-1

Gleeson, T., Wada, Y., Bierkens, M. F., & van Beek, L. P. (2012). Water balance of global aquifers revealed by groundwater footprint. *Nature*, *488*(7410), 197–200. https://doi.org/10.1038/nature11295

Grace, J., San Jose, J., Meir, P., Miranda, H. S., & Montes, R. A. (2006). Productivity and carbon fluxes of tropical savannas. *Journal of Biogeography*, *33*(3), 387–400. https://doi.org/10.1111/j.1365-2699.2005.01448.x

Gu, G., Adler, R. F., Huffman, G. J., & Curtis, S. (2007). Tropical rainfall variability on interannual-to-interdecadal and longer time scales derived from the GPCP monthly product. *Journal of Climate*, *20*(15), 4033–4046. https://doi.org/10.1175/JCLI4227.1

Held, I. M., & Soden, B. J. (2006). Robust responses of the hydrological cycle to global warming. *Journal of Climate*, *19*(21), 5686–5699. https://doi.org/10.1175/JCLI2990.1

Huang, J., Li, Y., Fu, C., Chen, F., Fu, Q., Dai, A., et al. (2017). Dryland climate change: Recent progress and challenges. *Reviews of Geophysics*, *55*, 719–778. https://doi.org/10.1002/2016RG000550

Huang, J., Yu, H., Guan, X., Wang, G., & Guo, R. (2016). Accelerated dryland expansion under climate change. *Nature Climate Change*, *6*, 166. https://doi.org/10.1038/nclimate2837

Humphrey, V., Gudmundsson, L., & Seneviratne, S. I. (2016). Assessing global water storage variability from GRACE: Trends, seasonal cycle, subseasonal anomalies and extremes. *Surveys in Geophysics*, *37*, 357–395. https://doi.org/10.1007/s10712-016-9367-1

Huxman, T. E., Smith, M. D., Fay, P. A., Knapp, A. K., Shaw, M. R., Loik, M. E., et al. (2004). Convergence across biomes to a common rain-use efficiency. *Nature*, *429*(6992), 651–654. https://doi.org/10.1038/nature02561

IPCC: Climate Change (2014). In Core Writing Team, R. K. Pachauri, & L. A. Meyer (Eds.), *Synthesis report. Contribution of Working Groups I, II and III to the Fifth Assessment Report of the Intergovernmental Panel on Climate Change* (p. 151). Geneva, Switzerland: IPCC.

Joodaki, G., Wahr, J., & Swenson, S. (2014). Estimating the human contribution to groundwater depletion in the Middle East, from GRACE data, land surface models and well observations. *Water Resources Research*, *50*, 2679–2692. https://doi.org/10.1002/2013WR014633

Junyan, Y., Zhou, X., Yi, S., & Sun, W. (2015). Determining dislocation love numbers using GRACE satellite mission gravity data. *Geophysical Journal International*, *203*, 257–269. https://doi.org/10.1093/gji/ggv265

Kamai, T., & Assouline, S. (2018). Evaporation from deep aquifers in arid regions: Analytical model for combined liquid and vapor water fluxes. *Water Resources Research*, *54*, 4805–4822. https://doi.org/10.1029/2018WR023030

Kumar, S., Allan, R. P., Zwiers, F., Lawrence, D. M., & Dirmeyer, P. A. (2015). Revisiting trends in wetness and dryness in the presence of internal climate variability and water limitations over land. *Geophysical Research Letters*, *42*, 10,867–10,875. https://doi.org/10.1002/2015GL066858

Landerer, F. W., & Swenson, S. C. (2012). Accuracy of scaled GRACE terrestrial water storage estimates. *Water Resources Research*, *48*, W04531. https://doi.org/10.1029/2011WR011453

Lau, W. K., & Kim, K. M. (2015). Robust Hadley circulation changes and increasing global dryness due to CO_2 warming from CMIP5 model projections. *Proceedings of the National Academy of Sciences*, *112*, 3630–3635. https://doi.org/10.1073/pnas.1418682112

Liu, C., Allan, R. P., & Huffman, G. J. (2012). Co-variation of temperature and precipitation in CMIP5 models and satellite observations. *Geophysical Research Letters*, *39*, L13803. https://doi.org/10.1029/2012GL052093

Long, D., Longuevergne, L., & Scanlon, B. R. (2015). Global analysis of approaches for deriving total water storage changes from GRACE satellites. *Water Resources Research*, *51*, 2574–2594. https://doi.org/10.1002/2014WR016853

Long, D., Scanlon, B. R., Longuevergne, L., Sun, A. Y., Fernando, D. N., & Save, H. (2013). GRACE satellite monitoring of large depletion in water storage in response to the 2011 drought in Texas. *Geophysical Research Letters*, *40*, 3395–3401. https://doi.org/10.1002/grl.50655

Mao, J., Shi, X., Thornton, P. E., Hoffman, F. M., Zhu, Z., & Myneni, R. B. (2013). Global latitudinal-asymmetric vegetation growth trends and their driving mechanisms: 1982–2009. *Remote Sensing*, *5*, 1484–1497. https://doi.org/10.3390/rs5031484

Middleton, N., & Thomas, D. (1997). *World atlas of desertification*. United Kingdom: Oxford University Press. Retrieved from https://wad.jrc.ec.europa.eu/patternsaridity

Niu, G. Y., Fang, Y.-H., Chang, L.-L., Jin, J., Yuan, H., & Zeng, X. (2020). Enhancing the Noah-MP ecosystem response to droughts with an explicit representation of plant water storage supplied by dynamic root water uptake. *Journal of Advances in Modeling Earth Systems*, *12*, e2020MS002062. https://doi.org/10.1029/2020MS002062

Niu, G. Y., & Yang, Z. L. (2004). Effects of vegetation canopy processes on snow surface energy and mass balances. *Journal of Geophysical Research*, *109*, D23111. https://doi.org/10.1029/2004JD004884

Niu, G. Y., & Yang, Z. L. (2006). Effects of frozen soil on snowmelt runoff and soil water storage at a continental scale. *Journal of Hydrometeorology*, *7*(5), 937–952. https://doi.org/10.1175/JHM538.1

Niu, G. Y., Yang, Z. L., Dickinson, R. E., Gulden, L. E., & Su, H. (2007). Development of a simple groundwater model for use in climate models and evaluation with Gravity Recovery and Climate Experiment data. *Journal of Geophysical Research*, *112*, D07103. https://doi.org/10.1029/2006JD007522

Niu, G. Y., Yang, Z. L., Mitchell, K. E., Chen, F., Ek, M. B., Barlage, M., et al. (2011). The community Noah land surface model with multiparameterization options (Noah-MP): 1. Model description and evaluation with local-scale measurements. *Journal of Geophysical Research*, *116*, D12109. https://doi.org/10.1029/2010JD015139

Palmer, P. I., & Smith, M. J. (2014). Earth systems: Model human adaptation to climate change. *Nature News*, *512*, 365–366. https://doi.org/10.1038/512365a

Phillips, T., Nerem, R. S., Fox-Kemper, B., Famiglietti, J. S., & Rajagopalan, B. (2012). The influence of ENSO on global terrestrial water storage using GRACE. *Geophysical Research Letters*, *39*, L16705. https://doi.org/10.1029/2012GL052495

Polson, D., Hegerl, G. C., Allan, R. P., & Sarojini, B. B. (2013). Have greenhouse gases intensified the contrast between wet and dry regions? *Geophysical Research Letters*, *40*, 4783–4787. https://doi.org/10.1002/grl.50923

Ponce-Campos, G. E., Moran, M. S., Huete, A., Zhang, Y., Bresloff, C., Huxman, T. E., et al. (2013). Ecosystem resilience despite large-scale altered hydroclimatic conditions. *Nature*, *494*, 349–352. https://doi.org/10.1038/nature11836

Poulter, B., Frank, D., Ciais, P., Myneni, R. B., Andela, N., Bi, J., et al. (2014). Contribution of semi-arid ecosystems to interannual variability of the global carbon cycle. *Nature*, *509*, 600–603. https://doi.org/10.1038/nature13376

Prăvălie, R. (2016). Drylands extent and environmental issues. A global approach. *Earth-Science Reviews*, *161*, 259–278. https://doi.org/10.1016/j.earscirev.2016.08.003

Reager, J. T., Gardner, A. S., Famiglietti, J. S., Wiese, D. N., Eicker, A., & Lo, M. H. (2016). A decade of sea level rise slowed by climate-driven hydrology. *Science*, *351*, 699–703. https://doi.org/10.1126/science.aad8386

Reynolds, J. F., Smith, D. M. S., Lambin, E. F., Turner, B. L., Mortimore, M., Batterbury, S. P., et al. (2007). Global desertification: Building a science for dryland development. *Science*, *316*(5826), 847–851. https://doi.org/10.1126/science.1131634

Richard Peltier, W., Argus, D. F., & Drummond, R. (2018). Comment on "An assessment of the ICE-6G_C (VM5a) glacial isostatic adjustment model" by Purcell et al. *Journal of Geophysical Research: Solid Earth*, *123*, 2019–2028. https://doi.org/10.1002/2016JB013844

Rodell, M., Famiglietti, J. S., Wiese, D. N., Reager, J. T., Beaudoing, H. K., Landerer, F. W., & Lo, M. H. (2018). Emerging trends in global freshwater availability. *Nature*, *557*, 651–659. https://doi.org/10.1038/s41586-018-0123-1

Rodell, M., Houser, P. R., Jambor, U. E. A., Gottschalck, J., Mitchell, K., Meng, C. J., et al. (2004). The global land data assimilation system. *Bulletin of the American Meteorological Society*, *85*(3), 381–394. http://doi.org/10.1175/BAMS-85-3-381

Rodell, M., Velicogna, I., & Famiglietti, J. S. (2009). Satellite-based estimates of groundwater depletion in India. *Nature*, *460*(7258), 999. https://doi.org/10.1038/nature08238

Safriel, U., Adeel, Z., Niemeijer, D., Puigdefabregas, J., White, R., Lal, R., & King, C. (2005). Dryland systems. In *Ecosystems and human well-being: Current state and trends: Findings of the condition and trends working group* (pp. 623–662). Washington, DC: Island Press.

Sakumura, C., Bettadpur, S., & Bruinsma, S. (2014). Ensemble prediction and intercomparison analysis of GRACE time-variable gravity field models. *Geophysical Research Letters*, *41*, 1389–1397. https://doi.org/10.1002/2013GL058632

Save, H., Bettadpur, S., & Tapley, B. D. (2016). High-resolution CSR GRACE RL05 mascons. *Journal of Geophysical Research: Solid Earth*, *121*, 7547–7569. https://doi.org/10.1002/2016JB013007

Scanlon, B. R., Longuevergne, L., & Long, D. (2012). Ground referencing GRACE satellite estimates of groundwater storage changes in the California Central Valley, USA. *Water Resources Research*, *48*, W04520. https://doi.org/10.1029/2011WR011312

Scanlon, B. R., Zhang, Z., Save, H., Sun, A. Y., Schmied, H. M., van Beek, L. P., et al. (2018). Global models underestimate large decadal declining and rising water storage trends relative to GRACE satellite data. *Proceedings of the National Academy of Sciences*, *115*, E1080–E1089. https://doi.org/10.1073/pnas.1704665115

Scanlon, B. R., Zhang, Z., Save, H., Wiese, D. N., Landerer, F. W., Long, D., et al. (2016). Global evaluation of new GRACE mascon products for hydrologic applications. *Water Resources Research*, *52*, 9412–9429. https://doi.org/10.1002/2016WR019494

Schimel, D. S. (2010). Drylands in the earth system. *Science*, *327*(5964), 418–419. https://doi.org/10.1126/science.1184946

Sheffield, J., Goteti, G., & Wood, E. F. (2006). Development of a 50-yr high-resolution global dataset of meteorological forcings for land surface modeling. *Journal of Climate*, *19*(13), 3088–3111. https://doi.org/10.1175/jcli3790.1

Shuttleworth, W. J. (2012). Daily estimates of evaporation. In *Terrestrial hydrometeorology* (pp. 179–197). UK: A John Wiley & Sons, Ltd., Publication.

Sun, W., & Zhou, X. (2012). Coseismic deflection change of the vertical caused by the 2011 Tohoku-Oki earthquake (*M*w 9.0). *Geophysical Journal International*, *189*(2), 937–955. https://doi.org/10.1111/j.1365-246X.2012.05434.x

Swenson, S. C. (2012). GRACE monthly land water mass grids NETCDF RELEASE 5.0. Ver. 5.0. PO.DAAC, CA, USA. Dataset accessed [2018-09-24] at https://dx.doi.org/10.5067/TELND-NC005

Swenson, S. C., & Wahr, J. (2006). Post-processing removal of correlated errors in GRACE data. *Geophysical Research Letters*, *33*, L08402. https://doi.org/10.1029/2005GL025285

Tapley, B. D., Bettadpur, S., Watkins, M. M., & Reigber, C. (2004). The gravity recovery and climate experiment: Mission overview and early results. *Geophysical Research Letters*, *31*, L09607. https://doi.org/10.1029/2004GL019920

Tellus (2019). TELLUS GRACE Level-3 1.0-degree Glacial Isostatic Adjustment v1.0 datasets produced by JPL. Ver. 1.0. PO.DAAC, CA, USA. Dataset accessed [2019-09-17] at https://doi.org/10.5067/GRGIA-1DJ10

Tiwari, V. M., Wahr, J., & Swenson, S. (2009). Dwindling groundwater resources in northern India, from satellite gravity observations. *Geophysical Research Letters*, *36*, L18401. https://doi.org/10.1029/2009GL039401

Trenberth, K. E. (2011). Changes in precipitation with climate change. *Climate Research*, *47*(1–2), 123–138. https://doi.org/10.3354/cr00953

van Dijk, A. I. J. M., Renzullo, L. J., & Rodell, M. (2011). Use of Gravity Recovery and Climate Experiment terrestrial water storage retrievals to evaluate model estimates by the Australian water resources assessment system. *Water Resources Research*, *47*, W11524. https://doi.org/10.1029/2011WR010714

Verseghy, D. L. (1991). CLASS—A Canadian land surface scheme for GCMs. I. Soil model. *International Journal of Climatology*, *11*(2), 111–133. https://doi.org/10.1002/joc.3370110202

Voss, K. A., Famiglietti, J. S., Lo, M., de Linage, C., Rodell, M., & Swenson, S. C. (2013). Groundwater depletion in the Middle East from GRACE with implications for transboundary water management in the Tigris-Euphrates-Western Iran region. *Water Resources Research*, *49*, 904–914. https://doi.org/10.1002/wrcr.20078

Wada, Y., van Beek, L. P. H., van Kempen, C. M., Reckman, J. W. T. M., Vasak, S., & Bierkens, M. F. P. (2010). Global depletion of groundwater resources. *Geophysical Research Letters*, *37*, L20402. https://doi.org/10.1029/2010GL044571

Wahr, J., & Zhong, S. (2012). Computations of the viscoelastic response of a 3-D compressible Earth to surface loading: An application to Glacial Isostatic Adjustment in Antarctica and Canada. *Geophysical Journal International*, *192*(2), 557–572. https://doi.org/10.1093/gji/ggs030

Wang, B., Liu, J., Kim, H.-J., Webster, P. J., & Yim, S.-Y. (2012). Recent change of the global monsoon precipitation (1979–2008). *Climate Dynamics*, *39*, 1123–1135. https://doi.org/10.1007/s00382-011-1266-z

Wang, L., D'Odorico, P., Evans, J. P., Eldridge, D. J., McCabe, M. F., Caylor, K. K., & King, E. G. (2012). Dryland ecohydrology and climate change: Critical issues and technical advances. *Hydrology and Earth System Sciences*, *16*(8), 2585–2603. https://doi.org/10.5194/hess-16-2585-2012

Wang, L., Shum, C. K., & Jekeli, C. (2012). Gravitational gradient changes following the 2004 December 26 Sumatra–Andaman earthquake inferred from GRACE. *Geophysical Journal International*, *191*(3), 1109–1118. https://doi.org/10.1111/j.1365-246X.2012.05674.x

Wang, P., Niu, G. Y., Fang, Y. H., Wu, R. J., Yu, J. J., Yuan, G. F., et al. (2018). Implementing dynamic root optimization in Noah-MP for simulating phreatophytic root water uptake. *Water Resources Research*, *54*, 1560–1575. https://doi.org/10.1002/2017WR021061

Wang, Y. H., Broxton, P., Fang, Y., Behrangi, A., Barlage, M., Zeng, X., & Niu, G. Y. (2019). A wet-bulb temperature-based rain-snow partitioning scheme improves snowpack prediction over the drier western United States. *Geophysical Research Letters*, *46*, 13,825–13,835. https://doi.org/10.1029/2019GL085722

Xu, L., Chen, N., Zhang, X., & Chen, Z. (2019). Spatiotemporal changes in China's terrestrial water storage from GRACE satellites and its possible drivers. *Journal of Geophysical Research: Atmospheres*, *124*, 11,976–11,993. https://doi.org/10.1029/2019JD031147

Yin, J. H. (2005). A consistent poleward shift of the storm tracks in simulations of 21st century climate. *Geophysical Research Letters*, *32*, L18701. https://doi.org/10.1029/2005GL023684

Yuan, R. Q., Chang, L. L., Gupta, H., & Niu, G. Y. (2019). Climatic forcing for recent significant terrestrial drying and wetting. *Advances in Water Resources*, *133*, 103425. https://doi.org/10.1016/j.advwatres.2019.103425

Zhu, Q., Riley, W. J., Tang, J. Y., Randerson, J. R., Collier, N., Hoffman, F. M., et al. (2019). Representing nitrogen, carbon, and phosphorus interactions in the ELMv1-ECA land model: Model development and global benchmarking, in revision JAMES.

Zhu, Z., Piao, S., Myneni, R. B., Huang, M., Zeng, Z., Canadell, J. G., et al. (2016). Greening of the Earth and its drivers. *Nature Climate Change*, *6*, 791–795. https://doi.org/10.1038/nclimate3004